Applied Catalysis B: Environmental 97 (2010) 398–406

Contents lists available at ScienceDirect

Applied Catalysis B: Environmental

journal homepage: www.elsevier.com/locate/apcatb

Flame-made $MgAl_{2-x}M_xO_4$ (M = Mn, Fe, Co) mixed oxides: Structural properties and catalytic behavior in methane combustion

Niels van Vegten, Tinku Baidya, Frank Krumeich, Wolfgang Kleist, Alfons Baiker*

Institute for Chemical and Bioengineering, Department of Chemistry and Applied Biosciences, ETH Zurich, Hoenggerberg, HCI, CH–8093 Zurich, Switzerland

ARTICLE INFO

Article history:
Received 1 February 2010
Received in revised form 16 April 2010
Accepted 26 April 2010
Available online 20 May 2010

Keywords:
$MgAl_{2-x}M_xO_4$ (M = Mn, Fe, Co) mixed oxides
Flame-spray pyrolysis
Spinel
Methane combustion

ABSTRACT

Spinel-like oxides with the general formula $MgAl_{2-x}M_xO_4$ (M = Mn, Fe, Co) were synthesized in a single step by flame-spray pyrolysis. High surface area materials were obtained, which showed improved resistance to sintering upon increasing the Al-content. XPS showed surface enrichment of the transition metal constituent, which favorably increased the fraction of transition metal exposed to the environment. By tuning the fraction of transition metal in the mixed oxide, materials were obtained with a good balance between thermal stability and activity in the catalytic combustion of methane. The activity of the materials increased in the order Fe < Co < Mn.

1. Introduction

Spinel-type oxides are compounds with the general chemical formula AB_2O_4. Generally, the A cation is tetrahedrally, and the B ion octahedrally coordinated, although inverse spinel structures are possible as well, in which B ions, partially or fully, occupy tetrahedral positions and A ions reside in the octahedral sites. Many elements can be accommodated in spinel or spinel-like structures which allows for a wide array of possible spinel formulations, and a correspondingly large flexibility for tailoring these oxides for specific applications. As such, spinels find use in many applications due to their optical, magnetic and (electro)chemical properties, examples of which are cathodes [1], sensors [2], phosphors in solid state lasers [3] as well as catalysts [4–26].

Spinel-catalyzed reactions include dry reforming of methane [15,17], steam reforming of methanol [10,14,24], methylation of phenol [4,13], decomposition of N_2O [16,25], oxidation of CO [11,18,20–21], methane [6,12] or other compounds [7,22–23], and reduction of NO with hydrocarbons [5,8–9,19,26]. Catalysts frequently feature Cu, Ni or Co as A cation and Al or transition metals such as Mn and Fe as B cation, although many other formulations can be found.

These materials are usually synthesized by co-precipitation or sol–gel method followed by high-temperature calcination. However, specific surface areas of these spinels are usually rather low, typically not exceeding 50 $m^2\,g^{-1}$ [5,8–9,13–14,18,20,23], limiting the catalytic potential of these materials.

Flame-spray pyrolysis [27] is an aerosol-based synthesis method of metal oxides which generally yields (mixed) metal oxides with high specific surface areas. It is very well suited for production of mixed metal oxides, and has been employed in the synthesis of perovskites (see [27] and references therein) and, to a lesser extent, spinels. These spinels include MAl_2O_4 oxides (M = Mg [28], Ni [29] and Zn [30]) and Li-based spinels [1]. However, to our knowledge, no catalytic studies were performed on these materials. In a recent study [31], FSP synthesis of a Pd-based combustion catalyst was reported, where the spinel acted as support.

Mostly binary spinels (i.e. two different cations) are reported in literature, and ternary systems ($AB_xB'_{2-x}O_4$) are only found sporadically [8,13,25,32–33]. Obviously, increasing the number of different cations poses a challenge with respect to phase purity; the tendency towards the formation of separate metal oxides in addition to the desired spinel is increasing with complexity of the system. Hence, such complex oxide systems require synthesis methods designed to produce well-mixed oxides.

Abatement of methane as by-product of various industrial processes has a greenhouse effect considerably larger than that of carbon dioxide. Also, the high-temperature combustion of methane in e.g. gas-turbines is prone to lead to generation of significant amounts of (thermal) NO_x with detrimental effects on human health and the environment [34]. By application of suitable combustion catalysts, the temperature of combustion can be

* Corresponding author. Tel.: +41 44 632 31 53; fax: +41 44 632 11 63.
E-mail address: baiker@chem.ethz.ch (A. Baiker).

0926-3373/$ – see front matter © 2010 Elsevier B.V. All rights reserved.
doi:10.1016/j.apcatb.2010.04.026

reduced, resulting in a decreased NO_x concentration in the exhaust gas.

There are several reports on applications of spinels in the catalytic combustion of methane [6,12,33,35–38], most of these dealing with spinels consisting of transition metals only. These spinels are based mainly on Cr, Co and Mn as active components. In some reports Al is incorporated as well in the spinel-like catalyst as in $CoAl_2O_4$ [38], or $MgMn_{0.25}Al_{1.75}O_4$ [33], or supporting the Co_3O_4 active phase in hydrotalcite derived spinels [36].

In this contribution the synthesis of $MgAl_{2-x}M_xO_4$ (M = Mn, Fe and Co, x = 0.1, 0.5, 1 and 2) spinel-like materials by flame-spray pyrolysis is presented. Mn, Fe and Co were chosen since these transition metals themselves form spinel phases readily and they show different activity for the combustion of methane, based on literature. The effect of the transition metal content on characteristics such as specific surface area and activity is discussed.

2. Experimental

2.1. Sample preparation

Magnesium(II) t-butoxide (technical quality, Fluka), aluminum(III) acetylacetonate (99%, ABCR), manganese(II) acetylacetonate (97%, Aldrich), iron(III) acetylacetonate (99+ % Acros), cobalt(III) acetylacetonate (98+ % Merck), acetic acid (analytical grade, Fluka) and methanol (analytical grade, Fluka) were used as received. The methanol/acetic acid mixture employed has been shown to yield materials with high initial specific surface area [31,39] and good resistance to sintering [31] compared to e.g. xylene-based materials [40]. Also, $MgAl_2O_4$ has already been synthesized from methanol/acetic acid solutions [31,41], demonstrating that spinel-like oxides can be prepared with this solvent mixture.

α-Al_2O_3 (99.5%; Strem Chemicals), used as inert diluent during methane combustion in the fixed bed reactor, was calcined at 900 °C for 3 h, crushed and sieved to obtain the 100–200 μm fraction.

The experimental set-up used for the flame-spray pyrolysis has been described in detail elsewhere [31,42]. In brief, flame-made $MgAl_{2-x}M_xO_4$ catalysts (M = Mn, Fe, Co; x = 0.1, 0.5, 1 and 2) were prepared by dissolving the appropriate amounts of the precursor salts in a 1:1 (vol%) mixture of acetic acid and methanol. The concentration of Mg was kept at 0.11 mol L^{-1} in all synthesis. Each solution was filtered over a glass filter, pumped through a capillary with 5 mL min^{-1} and nebulized with 5 L_n min^{-1} O_2. The resulting spray was ignited by a circular supporting methane/oxygen flame (1.5/0.9 L_n min^{-1}), resulting in an approximately 6 cm long flame. Particles were collected on a cooled Whatman GF6 filter (257 mm diameter). A Busch SV 1040C vacuum pump aided in particle recovery.

For reasons of comparison, $MgAl_2O_4$, Mn_3O_4, Fe_3O_4 and Co_3O_4 were synthesized as well according to the method described above.

2.2. Sample characterization

X-ray diffractograms were recorded on a Siemens D5000 using Cu Kα_1 (λ = 1.54056 Å) radiation in step mode between 15° and 65° 2θ with a step-size of 0.01° and 0.3 s $step^{-1}$.

Nitrogen physisorption isotherms (adsorption–desorption branches) were measured on a Micromeritics ASAP 2000 instrument at 77 K. Samples were outgassed under vacuum at 150 °C before measurement and the specific surface area (SSA) was determined using the BET method.

For (scanning) transmission electron microscopy ((S)TEM), the material was dispersed in ethanol and few drops were deposited onto a perforated carbon foil supported on a copper grid. TEM and STEM investigations were performed on a Tecnai F30 microscope (FEI; field emission cathode, operated at 300 kV, point resolution ~2 Å).

XPS analysis of the catalysts was performed on a Leybold Heraeus LHS11 MCD instrument using Al K_α (1486.6 eV) radiation. The sample was pressed into a sample holder, evacuated in a load lock to 10^{-6} mbar, and transferred to the analysis chamber (typical pressure <10^{-9} mbar). The peaks were energy-shifted to the binding energy of C 1s (284.8 eV [43]) to correct for the charging of the material. The surface composition of the catalysts was determined from the peak areas of Mg 2*s*, Al 2*p*, Mn 2*p*, O 1*s*, and C 1*s*, which were computed after subtraction of the Shirley-type background using empirically derived cross-section factors [44]. Note that Mg 2*p* could not be used for quantification due to exact overlap with Mn 3*p*.

Thermogravimetric (TG) experiments were performed on a Netzsch STA 449 C thermoanalyzer. Temperature Programmed Desorption (TPD) and Reduction (TPR) were performed on a thermoanalyzer with a flow of 50 mL min^{-1} He (TPD) or 50 mL min^{-1} 20% H_2/He (TPR) and a heating rate of 10 K min^{-1} from 30 to 950 °C. The difference graphs were obtained by subtraction of the TG-TPD trace from the TG-TPR trace.

2.3. Catalytic tests

The catalysts were pressed to pellets (at 3 tons, pellet diameter 1.4 cm resulting in a pressure of 1950 kg cm^{-2}), subsequently crushed and sieved, affording a 100–200 μm fraction. Typically, 100 mg of catalyst was diluted with 70 mg α-Al_2O_3 of 100–200 μm, shaken until a homogeneous mixture was obtained and subsequently loaded into a quartz u-tube reactor with an inner diameter of 5 mm, resulting in a bed of ca. 6 mm length. The catalyst bed was fixed by quartz wool plugs. The quartz u-tube was placed in a tubular oven (Carbolite Furnaces) and connected to a mass flow controller (Brooks, 5895E) and gas chromatograph (Hewlett Packard 6890N), equipped with GS-CarbonPLOT column and capable of automatic gas sampling.

Each catalytic experiment consisted of two cycles from 200 to 700 °C and back with heating and cooling rates of 2.5 K min^{-1}. Prior to each run, the catalyst was pre-treated for 1 h at 200 °C in the reaction mixture of 1 vol% CH_4, 4 vol% O_2, balance He. The total flow during each run was 130 mL min^{-1}, carbon dioxide and water were the only reaction products detected.

3. Results and discussions

3.1. Structural characteristics

The X-ray diffractograms of as-prepared $MgAl_{2-x}M_xO_4$ (x = 0.1, 0.5, 1 and 2, M = Mn, Fe or Co) materials are given in Fig. 1. The Al-containing samples had diffraction patterns closely resembling that of pure $MgAl_2O_4$ (JCPDS 05-0672), which persisted after calcining at 700 °C for 12 h. Similar diffractograms have been found for transition metal doped $MgAl_2O_4$ spinels [45]. $MgAlCoO_4$ formed an exception, however, and showed minor reflections which fitted with a (Mg,Co)O phase (JCPDS 02-1201) after calcining. Compared to pure $MgAl_2O_4$, the main spinel reflections of Mn and Fe substituted spinels were slightly shifted to lower values of 2θ with increasing amount of transition metal. The peak positions of the Co-based spinels were independent of transition metal loading. This fits well with the effective ionic radii of the elements employed [46]: octahedrally coordinated Mn^{3+} and Fe^{3+} have radii of 0.65 and 0.645 Å (both high spin), respectively, larger than those of Co^{3+} (low spin) and Al^{3+}, which are 0.525 and 0.53 Å, respectively. The

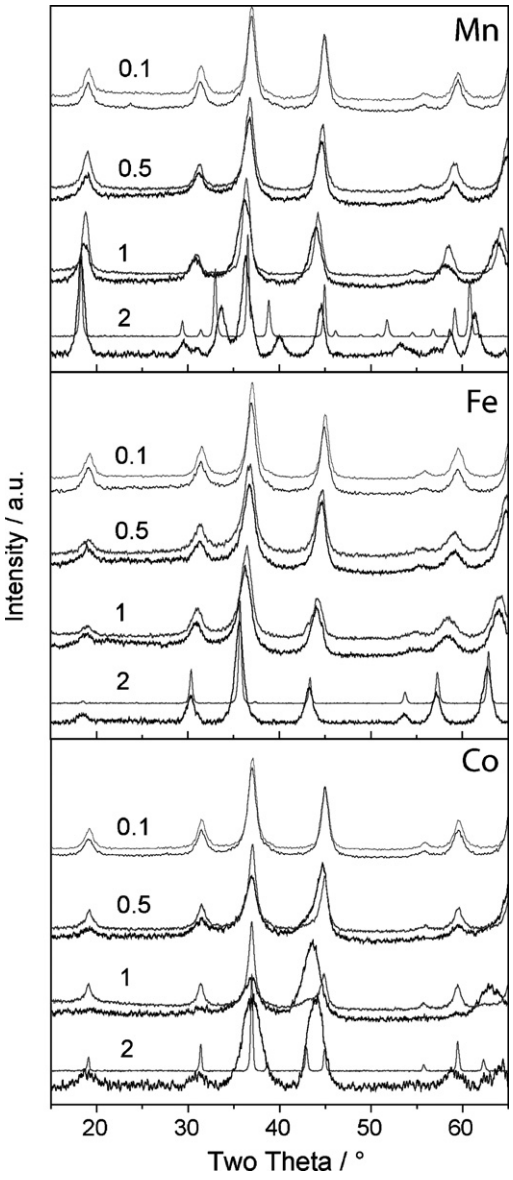

Fig. 1. Powder XRD diffraction patterns of as-prepared (black) and calcined (grey) spinel-like oxides. The patterns are presented with an off-set for better visualization, with the values of the substitution degree x indicated above.

crystallite sizes estimated by applying the Scherrer formula to the (3 1 1) reflections are listed in Table 1.

The Al-free materials had diffraction patterns which showed less resemblance with that of $MgAl_2O_4$. For $MgMn_2O_4$ the as-prepared material had a diffraction pattern very similar to that of a $MgMn_2O_4$ spinel (JCPDS 023-0392) which altered slightly upon calcination at 700 °C for 12 h, and fitted well with another $MgMn_2O_4$ spinel phase (JCPDS 01-072-1336). $MgFe_2O_4$ displayed a good fit with the magnesioferrite spinel phase (JCPDS 01-073-1960), and calcining resulted in narrowing of these reflections. $MgCo_2O_4$ showed broad reflections, and the positions of the reflections fitted well to an inverse spinel phase, $(Mg_{0.23}Co_{0.77})(Mg_{0.35}Co_{1.65})O_4$ (JCPDS 01-081-0668). However, a good fit with Co_3O_4 (JCPDS 09-0418) was also obtained, although the absence of any Mg-related reflections suggests the formation of the Mg-Co inverse spinel instead. The broad reflection could also hint at the presence of a (Co,Mg)O phase. Calcining resulted in narrowing of the reflections, and the large reflection around 44° 2θ splitted into two smaller reflections around 42° and 45° 2θ. The resulting diffraction pattern fitted well with $(Mg_{0.18}Co_{0.82})(Mg_{0.2}Co_{1.8})O_4$ (JCPDS 01-081-0667), also an inverse spinel phase, although reflections at 62.3°, 42.8° and 36.8° 2θ indicated the presence of a (Co,Mg)O phase, as in the $MgAlCoO_4$ sample.

Table 1
Material characteristics of spinel-like oxides; XRD-derived crystallite sizes (d_{XRD}), BET specific surface area (SSA), and onset temperature of reduction.

Sample	d_{XRD}[a] (nm)	SSA ($m^2\,g^{-1}$)	Onset of reduction (°C)
Mn_3O_4			310/–[c]
$MgMn_2O_4$	9 (32)[b]	144 (31)	305/–
$MgAlMnO_4$	6 (11)	174 (121)	335/–
$MgAl_{1.5}Mn_{0.5}O_4$	6 (9)	185 (167)	345/–
$MgAl_{1.9}Mn_{0.1}O_4$	9 (9)	176 (173)	435/–
Fe_3O_4			240/380
$MgFe_2O_4$	9 (30)	182 (72)	230/460
$MgAlFeO_4$	6 (10)	176 (146)	255/600
$MgAl_{1.5}Fe_{0.5}O_4$	6 (7)	188 (185)	315/655
$MgAl_{1.9}Fe_{0.1}O_4$	9 (9)	182 (146)	420/625
Co_3O_4			190/260
$MgCo_2O_4$	4 (36)	129 (11)	185/415
$MgAlCoO_4$	5 (13)	176 (135)	190/550
$MgAl_{1.5}Co_{0.5}O_4$	6 (10)	191 (165)	220/590
$MgAl_{1.9}Co_{0.1}O_4$	9 (9)	180 (137)	235/590
$MgAl_2O_4$	9 (9)	212 (177)	–

[a] Crystallite sizes estimated from the line broadening of (3 1 1) reflection.
[b] Number between brackets indicates sample after calcining at 700 °C for 12 h.
[c] Second number indicates onset of second reduction step (if present).

Calcination at 700 °C for 12 h resulted predominantly in narrowing of the reflections, and generally no new phases were observed after this high-temperature treatment. The narrowing of the reflections indicated crystallite growth, the degree of which was greatly dependent on the fraction of transition metal in the sample. Crystallite sizes increased from 5–10 nm for the as-prepared materials to 10–35 nm after calcination (see Table 1). Generally, the tendency towards sintering increased with higher loading of the transition metal. For comparison, the crystallite size of pure $MgAl_2O_4$ was unaffected by calcining.

The influence of high-temperature treatment on the morphology of the spinel-like oxides was also reflected by the specific surface area determined by the BET method (Table 1). For as-prepared materials surface areas were between 145 and 185 (Mn), 175 and 190 (Fe) and 130 and 190 (Co) $m^2\,g^{-1}$, generally increasing with decreasing transition metal content. These values are comparable with the highest surface areas for spinels found in literature [1,12,17,47]. The surface area decreased after calcination at 700 °C for 12 h, yielding SSAs between 30 and 175 (Mn), 70 and 185 (Fe) and 10 and 165 (Co) $m^2\,g^{-1}$ (see Table 1). This behavior is graphically presented in Fig. 2 where the resistance to sintering, expressed as the surface area retained after calcination (in %), is shown. Little surface was retained for those materials containing only transition metal in the B-position, and this value increased with decreasing transition metal content. $MgAl_2O_4$ showed only a moderate decrease of SSA, decreasing from 210 to 180 $m^2\,g^{-1}$ (a ca. 17% decrease). This loss is comparable with that of the transition metal containing materials with $x = 0.1$ and 0.5, indicating that the thermal stability was not increased significantly by further decrease of the transition metal content.

Analysis of the pore size distribution by recording full nitrogen adsorption and desorption isotherms (see insert in Fig. 2) revealed that the flame-made materials were virtually non-porous. The hysteresis behavior observed at high relative pressure show some macroporosity due to voids between the primary particles. Similar behavior has been reported before for high-surface area flame-made materials [39].

Transmission electron microscopy (TEM) analysis was performed on as-prepared Mn-based spinels. These materials

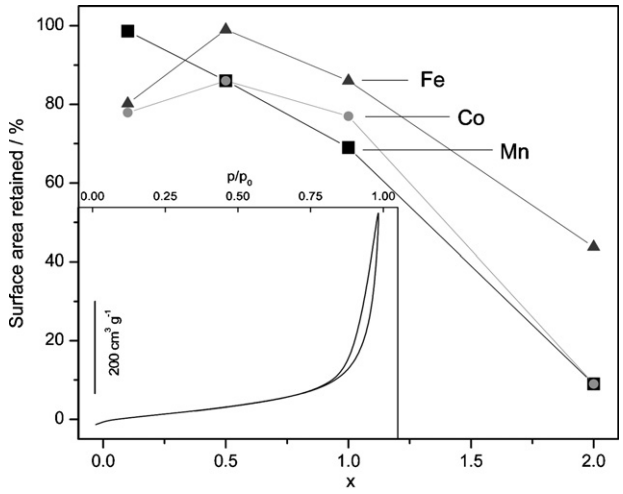

Fig. 2. Dependence of specific surface area retained after thermal treatment (700 °C, 12 h) on the substitution degree *x*. The insert shows a typical adsorption–desorption isotherm ($MgAlFeO_4$).

consisted of particles in the range of 6–15 nm (Fig. 3), in the same range as the average crystallite size derived by XRD. At high magnification (ca. 60 nm × 60 nm), lattice fringes could be observed on many particles. Based on similarity in particle and crystallite size, and the presence of lattice fringes, we conclude that the majority of the material was present in the form of mono-crystalline particles.

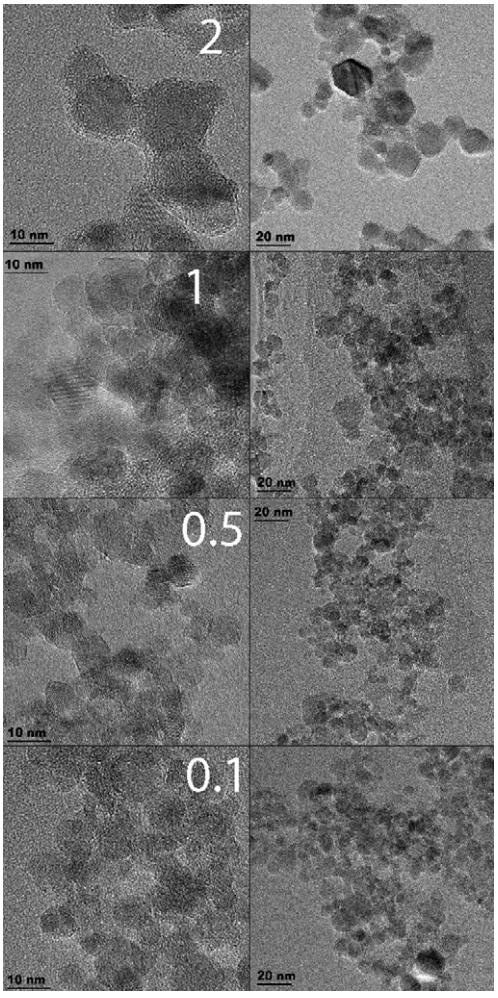

Fig. 3. TEM images of as-prepared Mn-based spinel-like oxides.

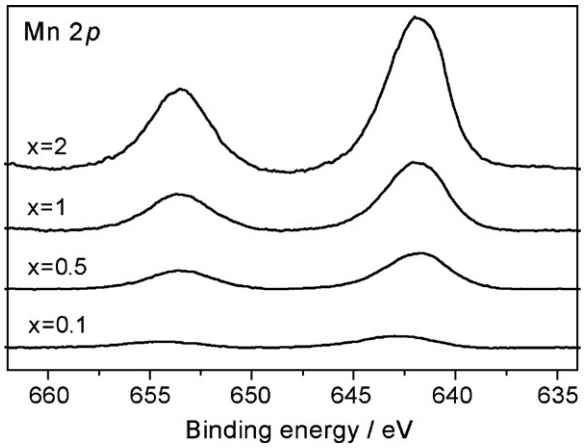

Fig. 4. XPS spectra of $MgAl_{2-x}Mn_xO_4$ ($x = 0.1, 0.5, 1$ and 2) showing the Mn 2*p* binding energies.

3.2. Bulk and surface composition

From XRD analysis it appeared that FSP synthesis resulted in a rather homogeneous distribution of the elements as no other phases were detected besides the desired spinel structure. However, the use of XRD is limited to crystalline solids, and a certain crystallite size is required in order to obtain distinct diffraction. Thus, based on XRD alone, the presence of XRD-amorphous material with different composition cannot be excluded. TEM analysis of the materials showed no particles smaller than 5 nm (i.e. XRD-amorphous) or other phases different from the crystalline solids found throughout the material. To assess the distribution of the elements in the material, energy dispersive X-ray spectroscopy (EDXS) was performed on Mn-based spinels. On a ca. 50 nm × 50 nm scale, EDXS showed minor variations in Mg, Mn and Al concentration, although these variations were too small to suggest large segregation of the material. Higher magnifications were not possible due to poor signal to noise ratio.

Based on XRD, TEM and EDXS analysis we conclude that the flame-made oxides all showed spinel structure and consisted of mono-crystalline particles. And apart from the indications of a (Co,Mg)O phase in as-prepared $MgAlCoO_4$ and calcined $MgCo_2O_4$, no evidence for segregated phases was found. However, the materials have experienced rather high temperatures for relatively short times during flame-synthesis [27] in an environment rich in carbon dioxide and water. Under these conditions, the surface composition might differ from that of the bulk. To study the surface composition, XPS analyses of the as-prepared Mn-based materials were performed. Table 2 lists the peak positions and the relative concentrations of the metal cations.

Peak positions of Mg *2s* (taken instead of Mg *2p* due to its overlap with Mn *3p*) and Al 2*p* were around 88.1 and 73.5 eV, respectively, for Mn-rich samples ($x = 2$, 1 and 0.5). The fact that the binding energies were smaller than expected could be explained by a significant amount of hydroxyl groups present at the surface [48–49]. For $x = 0.1$, these values were 88.8 and 74.3 eV for Mg *2s* and Al 2*p*, respectively, being in better agreement with literature reports on spinels [50]. The Mn 2*p* peaks are shown in Fig. 4. The Mn 2*p* 3/2 peak was around 641.9 eV for $x = 2$–0.5, in line with Mn^{2+} and Mn^{3+} species [51–53]. The rather high binding energy of $Mn_{0.1}$ at 642.8 eV, could indicate the co-existence of higher oxidized Mn-species on the spinel surface [51,53].

Table 2
XPS binding energies and cation concentration of Mn-based spinel-like oxides.

Sample	Mn $_{2p3/2}$ eV	Mn %	Al $_{2p}$ eV	Al %	Mg $_{2s}$ eV	Mg %
$MgMn_2O_4$	641.9	70 (66.7)[a]	–	0 (0)	88.2	30 (33.3)
$MgAlMnO_4$	642.0	43/53[b] (33.3)	73.5	20/16 (33.3)	88.0	37/30 (33.3)
$MgAl_{1.5}Mn_{0.5}O_4$	641.8	32/34 (16.7)	73.5	41/34 (50)	88.1	27/32 (33.3)
$MgAl_{1.9}Mn_{0.1}O_4$	642.8	8 (3.3)	74.3	60 (63)	88.8	33 (33.3)

[a] Numbers in brackets indicate the theoretical value assuming bulk composition.
[b] Numbers under the slash indicate the values obtained after calcining the sample at 700 °C for 12 h.

Integration of the peaks gave information on the availability of different elements on the surface. As can be expected, the relative concentration (expressed as percentage of total metal cations) of Mn decreased with decreasing Mn content (from 70% for $x = 2$ to 6% for $x = 0.1$). Vice versa, the relative concentration of Al increased (from 0 to 60%). The concentration of Mg remained rather constant around its nominal value of 33.3%. A light scatter was observed, which is likely due to the fact that the Mg *2s* peak was used for quantification of the Mg signal instead of the Mg *2p*, due to superposition of the Mn *3p* peak. The concentrations of the cations on the surface, as well as their expected values, are listed in Table 2.

Fig. 5 shows the relative concentration of transition metal (TM) as function of the substitution degree *x*. With increasing Mn content, Al showed concentrations of 60–20%, indicating a deficiency at the surface of 5–40%, respectively. Manganese increased monotonously with increasing substitution degree, as could be expected. However, its surface concentration was more than twice that of the expected value at $x = 0.1$, indicating substantial enrichment. At higher substitution degree, the enrichment decreased, reaching an enrichment of around 5% for $x = 2$.

Two conclusions can be drawn from these values. Firstly, the surface compositions of these materials did not correspond to that of the bulk and deficiencies (particularly in Al) and enrichments (particularly Mn) were found relative to the bulk. Secondly, incorporation of Al had a significant effect on the surface concentration of Mn: from a 5% enrichment the surface became more and more enriched the higher the fraction of Al in the B position was.

The higher relative loss in surface area of $MgMn_2O_4$ compared to $MgAl_2O_4$ (*vide supra*) inferred a lower melting point of the former compared to the latter, related to the lower lattice energy. Thus, it is not surprising that the former components were enriched on the surface. From thermodynamic considerations, the element or elements forming the most stable oxide will be located in the centre of the particle, whereas those elements forming less stable bonds will be located on the outside of the particle. The most stable configuration will be that where the strongest bonds are predominantly located within the particle and the weakest possible bonds are thus located on the outside. In this case, this will lead to Mn surface enrichment in the as-prepared particles.

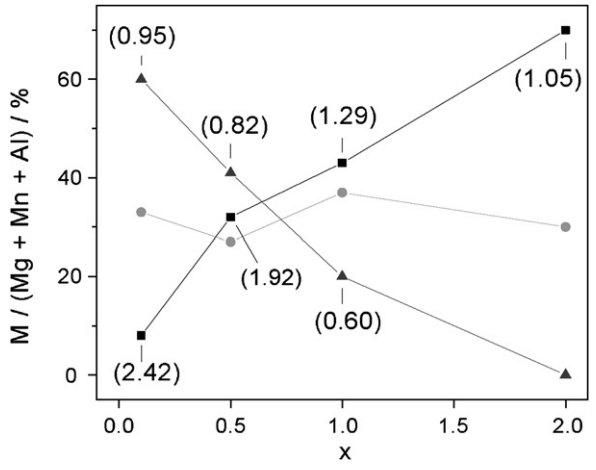

Fig. 5. The concentration of Mg (light-grey circles), Al (grey triangles) and Mn (black squares) on the surface of Mn-based spinel-like oxides as function of the substitution degree *x*. The numbers in brackets indicate the ratio of the measured and nominal concentrations.

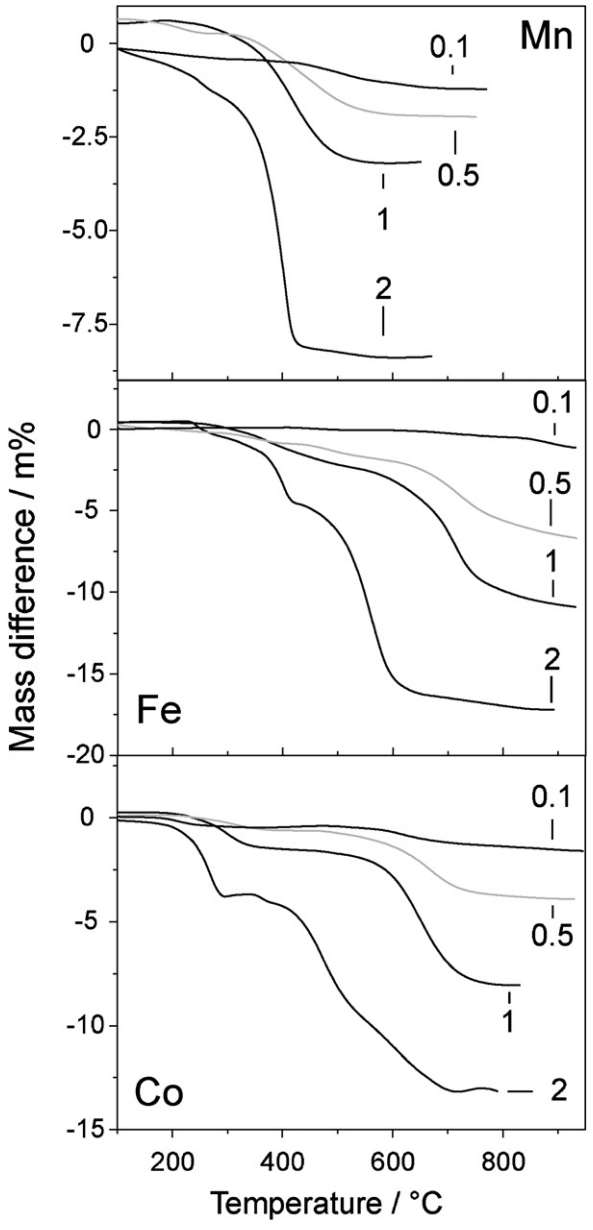

Fig. 6. Temperature programmed reduction of the spinel oxides as mass difference graphs of the TPD and TPR experiment.

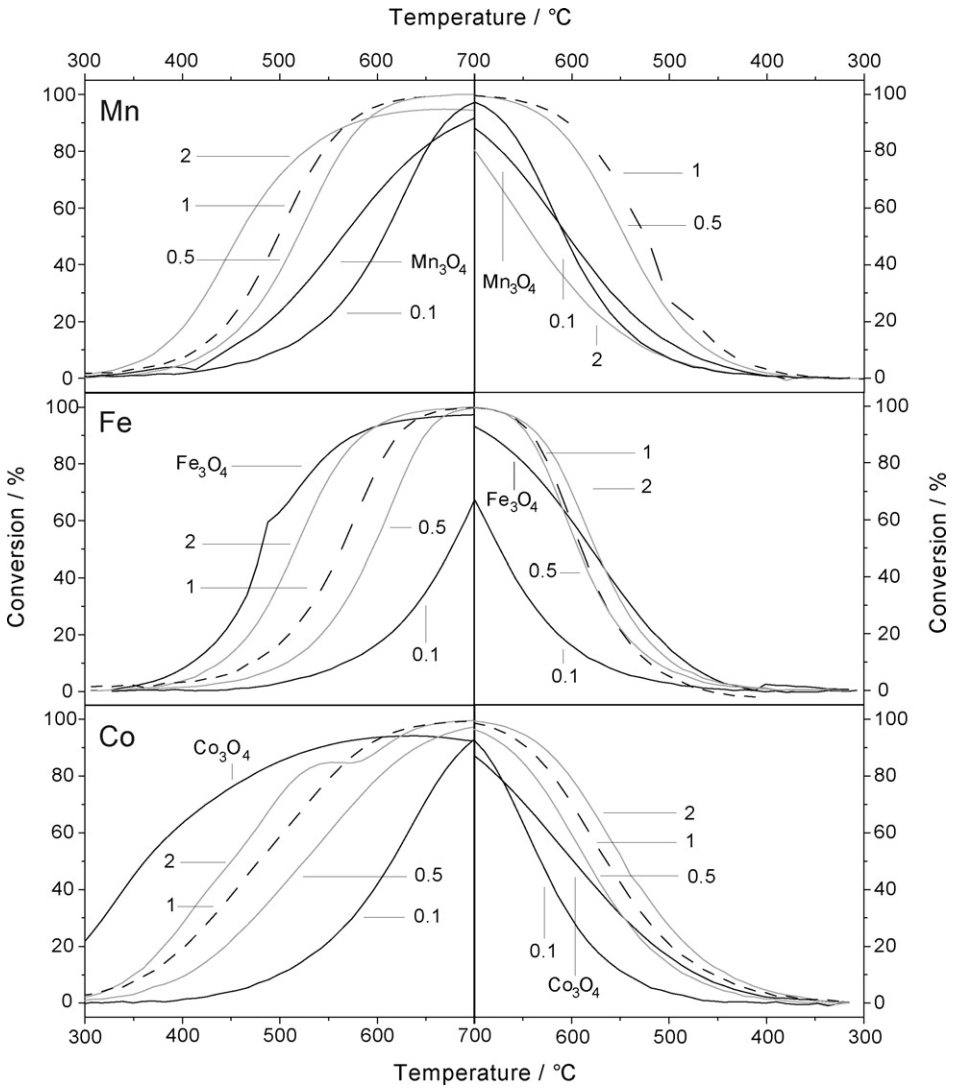

Fig. 7. Conversion of methane as function of temperature. The first cycle of each material is shown, consisting of heating (left) and cooling (right).

Calcined samples (700 °C) showed also surface enrichment of Mn (see Table 2), in fact, the Mn concentration increased for $MgAlMnO_4$ after calcining. This suggests that this enrichment plays an important role over a wide temperature range. Hence, less of the valuable transition metal will be located in the bulk of the particle and a larger fraction of the transition metal can participate in the reaction.

3.3. Reducibility of the spinel-based oxides

The reducibility of transition metals is frequently taken to characterize the redox properties of the material [4,7]. The reducibility of the spinels was assessed by performing a TPR and a TPD on as-prepared materials and subsequent subtraction of their TG traces (see experimental section for details). This cancelled out the effect of desorption of adsorbed species (water and carbon dioxide, as evidenced by MS, not shown) without the need for pre-treatment at elevated temperature, possibly altering the sample. The resulting mass difference graphs are depicted in Fig. 6.

The reduction of Mn was a one step process as reported for Mn_3O_4 oxides [54], and resulted from the reduction of Mn^{3+} to Mn^{2+}. The reduction of Fe and Co on the other hand showed two distinct steps: the first step was reduction of M^{3+} to M^{2+}, followed by reduction of M^{2+} to M^0. A two-step reduction for Fe- [55] and Co-oxides [56] has been reported before. Pure Mn-, Fe- and Co-oxides (all in the form of their respective spinel phases, not shown) showed a reduction pattern similar to that of their respective MgM_2O_4 analogues.

The onset of reduction of the spinel-like oxides as well as their second reduction step (only for Fe- and Co-based spinels) are presented in Table 1. Reduction started between 305 and 435 °C (Mn), 230 and 420 °C (Fe) and 185 and 235 °C (Co). The order in which the transition metals reduce over the entire substitution range was Co < Fe ≤ Mn. The data show that with increasing Al-content, the onset of reduction shifted to higher temperatures. Similar behavior was reported for Al_2O_3 supported Mn, where the onset of reduction decreased with increasing Mn-loading [57]. Also, the full transition metal spinels (Mn_3O_4, Fe_3O_4 and Co_3O_4) showed a similar onset of reduction compared to their Mg-containing counterparts. This indicates that the presence of Mg did not greatly alter the reducibility of the transition metal.

The start of the second reduction step was between 380 and 835 °C (Fe) and 260 and 590 °C (Co). Also here, a clear influence of the Al-content on the start of the second reduction step was observed. In contrast to the onset of reduction, however, the Mg-based spinels seemed to have a higher temperature at which the second reduction step starts compared to the pure transition metal oxides. Possibly, Mg is stabilizing Fe and Co in their +2 oxidation

states by formation of mixed oxides, leading to higher temperatures of reduction, as observed for (Mg,Co)O [58].

The dependency of the onset of reduction on the TM substitution degree hints at TM species with different stability. Since for each element the lowest reduction temperature was found for the full TM spinels, the close vicinity of transition metals likely enhanced the reducibility of that material due to decreasing the strength of the metal-oxide bond. Introduction of Al led to an increased stability and thus to a higher onset of reduction.

3.4. Activity of the spinel-based oxides

The activity of the spinel-like oxides in methane combustion was assessed by performing cycles, each consisting of heating from 200 to 700 °C followed by cooling to 200 °C. At least two cycles were performed on each catalyst, and if no or minimal changes were observed between two consecutive cooling half-cycles, the material was deemed stable.

Fig. 7 shows the conversion profiles obtained during the first cycle for the $MgAl_{2-x}M_xO_4$ materials. The pure transition metal spinels (Mn_3O_4, Fe_3O_4 and Co_3O_4) are included for comparison. In general, standard s-type curves were obtained for all catalysts except $MgCo_2O_4$ and Co_3O_4, where during heating a decrease of conversion was obtained above 500 and 600 °C, respectively, possibly due to strong sintering of these samples. During the first cycle, the conversion could be directly linked to the TM substitution degree: the higher the TM substitution, the higher the conversion. However, during cooling a different behavior arose, and such correlation was no longer present. This was especially observed for the pure transition metal spinels, which in case of Fe and Co were significantly more active compared to their Mg- and Al-containing counterparts during heating. After high-temperature treatment however, these materials showed much less activity.

To better analyze this behavior, the activity of the samples was expressed in terms of light-off temperature (here defined as temperature at 5% conversion, or $T_{5\%}$), temperature at 50% conversion ($T_{50\%}$) and reaction rate at 550 °C (r_{550}). The initial light-off temperatures ranged from 348 to 454 °C (Mn), 412 to 527 °C (Fe) and 314 to 462 °C (Co) and were consistently increasing with increasing Al-content which is presented in Fig. 8A. The $T_{5\%}$ (Fig. 8A) showed a behavior similar to the onset of reduction in Table 1: there was a trend to lower $T_{5\%}$ with increasing TM content, and the lowest light-off temperatures were obtained for Co, followed by Mn and Fe. This similarity could indicate a relation between the reducibility and (initial) activity of the material, which has already been suggested for transition metal based catalysts for methane combustion [35].

After high-temperature treatment higher $T_{5\%}$ were obtained (Fig. 8A, grey symbols). The difference between the initial value of $T_{5\%}$ and that obtained after high-temperature treatment was especially large for materials with a high TM content, and decreased for lower TM substitution degrees, until at a substitution degree of 0.1, the difference amounted to ca. 50 °C for Co, 20 °C for Mn and 10 °C for Fe.

The initial temperature of 50% conversion, $T_{50\%}$ (Fig. 8B), ranged from 457 to 607 °C (Mn), 515 to 674 °C (Fe) and 446 to 616 °C (Co). The $T_{50\%}$ showed a similar trend as the $T_{5\%}$ with respect to the activity, and a higher Al-content resulted in a higher $T_{50\%}$. The lowest initial $T_{50\%}$ was observed at 446 °C for $MgCo_2O_4$. However, after high-temperature treatment, $MgAlMnO_4$ was the most active material with a $T_{50\%}$ of 525 °C. Taking $T_{50\%}$ as a measure for the activity, a short overview on spinel-based methane combustion catalysts is presented in Table 3. Although catalyst formulations, methane to air ratio and the gas hourly space velocity (GHSV) vary greatly within this table (see caption Table 3), these data provide a rough comparison of activity of these catalysts. Note

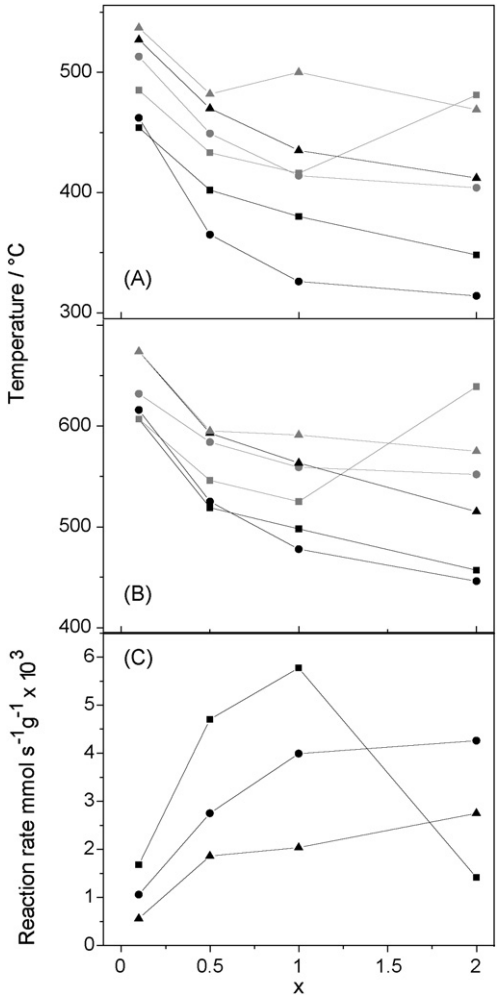

Fig. 8. Activity characteristics of the spinel-like oxides: $T_{5\%}$ (A), $T_{50\%}$ (B) and rate at 550 °C (C) determined from the conversion at 550 °C, after high-temperatur treatment (i.e. during the second or third cycle). The initial (black) values and those after treatment (grey) are shown for Mn (squares), Fe (triangles) and Co (circles). The reaction rate was determined after high-temperature treatment.

that the values presented in Table 3 were interpolated where necessary.

At a first glance, many values for $T_{50\%}$ appear lower than those presented in Fig. 8B. This might be partially explained by the conditions employed in these different studies, for example the GHSV employed in the current study was roughly twice as high compared to others [12,35,37] and the O_2/CH_4 ratio in the feed gas was relatively low [6,12,33,35–36]. The effect of the O_2/CH_4 ratio can be seen in the entries of [37], where an increase of this ratio from 3 to 40 resulted in a shift of the $T_{50\%}$ of ca. 50 °C (in brackets). In those cases where a direct comparison of catalyst formulation was possible (Mn_3O_4, Co_3O_4 and $MgFe_2O_4$), the values of $T_{50\%}$ obtained after high-temperature treatment (except Co_3O_4) were comparable with those obtained in other studies. Also, for $MgAl_{1.9}Mn_{0.1}O_4$ and $MgAl_{1.5}Mn_{0.5}O_4$, $T_{50\%}$ was 607 and 546 °C, respectively. These values are significantly lower than the $T_{50\%}$ of 960 °C obtained in [33], where a $MgAl_{1.75}Mn_{0.25}O_4$ catalyst was used.

Fig. 8A and B show that the largest differences in $T_{5\%}$ and $T_{50\%}$ were observed for those samples which also showed the largest decrease in specific surface area after high-temperature treatment (*vide supra*). Clearly, those materials with a rather low resistance to sintering will experience a relatively large loss of activity expressed in higher values of $T_{5\%}$ and $T_{50\%}$. Based on Fig. 8A and B, Mn-based spinels seemed to emerge as most stable and active compared to

Table 3
Overview of activity of spinel-based catalysts in the catalytic combustion of methane. Data have been interpolated where necessary.

Material	$T_{50\%}$ (°C)	Reference
Mn_3O_4	600	a
	604	This work
$MnCr_2O_4$	380 (330)	b
$Mg\,Al_{1.75}Mn_{0.25}O_4$	960	c
$MgFe_2O_4$	480	a
	580 (532)	b
	567	This work
Co_3O_4	485	a
	297	e
	597	This work
Co_3O_4/Al_2O_3	491	d
$CoCr_2O_4$	380	a
	375 (327)	b
$Co_{2.7}Mn_{0.3}O_4$	293	e
$Co_{2.5}Mn_{0.5}O_4$	306	e
$Co_{0.8}Cr_2O_4$	369 (321)	b
$CoFe_2O_4$	549 (498)	b
$CoAl_2O4$	10% at 707 °C	f
$CuCr_2O_4$ (mainly)	610	g

[a] 0.4 vol% CH_4:10 vol% O_2, 40,000 mL h^{-1} g^{-1} [35].
[b] 2.5 vol% CH_4:7.5 vol% O_2, or 0.4 vol% CH_4:10 vol% O_2 (between brackets) 29,880 mL h^{-1} g^{-1} [37].
[c] 0.5 vol% CH_4:8 vol% O_2, 100,000 h^{-1} [33].
[d] 1 vol% CH_4:19.8 vol% O_2, 60,000 h^{-1} [36].
[e] 1 vol% CH_4:10 vol% O_2, 36,000 mL h^{-1} g^{-1} [12].
[f] 1 vol% CH_4:4 vol% O_2, 135,000 h^{-1} [38].
[g] 1 vol% CH_4:6 vol% O_2, 23,500 h^{-1} [6].
This work: 1 vol% CH_4:4 vol% O_2, 78,000 mL h^{-1} g^{-1}.

Fe- or Co-based spinels. To better illustrate this, the rate of methane conversion at 550 °C, r_{550}, is presented in Fig. 8C.

After high-temperature treatment, the r_{550} ranged from 0.6×10^{-3} mmol s^{-1} g^{-1} for $MgAl_{1.9}Fe_{0.1}O_4$ to 5.8×10^{-3} mmol s^{-1} g^{-1} for $MgAlMnO_4$. In general, upon increasing the TM content r_{550} increased as well. The increase was not linear and flattened at higher TM content (Fe and Co) or even dropped at the maximal substation degree (Mn).

The general view that arises from Fig. 8 is that the higher the TM content in the sample, the higher the initial activity. However, part of this high activity was lost after successive cycling. This can be attributed to the low resistance to sintering of these materials compared to Al-containing catalysts, which reduced their catalytic potential. Mixing the rather active transition metal containing spinel with $MgAl_2O_4$, a spinel with good resistance to sintering resulted in materials with lower activity, but higher resistance to sintering.

4. Conclusions

Spinel-like oxides, with the formula $MgAl_{2-x}M_xO_4$ ($x = 0.1$, 0.5, 1 and 2, M = Mn, Fe or Co) have been prepared by single step flame-spray pyrolysis. These materials appeared single phase by X-ray diffraction. Electron microscopy showed the material to consist of mono-crystalline particles of 6 to 15 nm in diameter.

XPS indicated a certain degree of surface enrichment dependent on the transition metal constituent. Due to this enrichment, less of the valuable transition metal was buried in the bulk, allowing a higher percentage to participate in the reaction.

The onset of reduction of the transition metals depended on their substitution degree, indicating the formation of oxygen species with different stability.

Aluminum free spinels ($x = 2$) possessed good initial activity in the catalytic combustion of methane, but the low thermal stability of these materials significantly reduced their catalytic applicability. By introducing Al ($x = 0.1$, 0.5 and 1), the initial activity decreased, but a concurrent increase in thermal stability resulted in materials with almost similar (Fe, Co) or even superior (Mn) catalytic activity after conditioning.

Acknowledgements

We kindly acknowledge financial support by ETH Zurich (TH-09 06-2). Electron microscopy was performed at EMEZ (Electron Microscopy ETH Zurich).

References

[1] F.O. Ernst, H.K. Kammler, A. Roessler, S.E. Pratsinis, W.J. Stark, J. Ufheil, P. Novak, Mater. Chem. Phys. 101 (2007) 372–378.
[2] L. Satyanarayana, C.P.G. Reddy, S.V. Manorama, V.J. Rao, Sens. Actuators B-Chem. 46 (1998) 1–7.
[3] Y.X. Li, P.J. Niu, L. Hu, X.W. Xu, C.C. Tang, J. Lumin. 129 (2009) 1204–1206.
[4] N. Ballarini, F. Cavani, S. Passeri, L. Pesaresi, A.F. Lee, K. Wilson, Appl. Catal. A: Gen. 366 (2009) 184–192.
[5] L.Y. Chen, T. Horiuchi, T. Mori, Appl. Catal. A: Gen. 209 (2001) 97–105.
[6] G. Comino, A. Gervasini, V. Ragaini, Z.R. Ismagilov, Catal. Lett. 48 (1997) 39–46.
[7] F.G. Duran, B.P. Barbero, L.E. Cadus, C. Rojas, M.A. Centeno, J.A. Odriozola, Appl. Catal. B: Environ. 92 (2009) 194–201.
[8] G. Ferraris, G. Fierro, M. Lo Jacono, M. Inversi, R. Dragone, Appl. Catal. B: Environ. 45 (2003) 91–101.
[9] G. Fierro, M. Lo Jacono, M. Inversi, R. Dragone, G. Ferraris, Appl. Catal. B: Environ. 30 (2001) 173–185.
[10] S. Kameoka, T. Tanabe, A.P. Tsai, Catal. Lett. 100 (2005) 89–93.
[11] C. Laberty, C. Marquez-Alvarez, C. Drouet, P. Alphonse, C. Mirodatos, J. Catal. 198 (2001) 266–276.
[12] J.H. Li, X. Liang, S.C. Xu, J.M. Hao, Appl. Catal. B: Environ. 90 (2009) 307–312.
[13] T. Mathew, N.R. Shiju, K. Sreekumar, B.S. Rao, C.S. Gopinath, J. Catal. 210 (2002) 405–417.
[14] J. Papavasiliou, G. Avgouropoulos, T. Ioannides, Catal. Commun. 6 (2005) 497–501.
[15] A.L. Pinheiro, A.N. Pinheiro, A. Valentini, J. Mendes, F.F. de Sousa, J.R. de Sousa, M.D.C. Rocha, P. Bargiela, A.C. Oliveira, Catal. Commun. 11 (2009) 11–14.
[16] N. Russo, D. Fino, G. Saracco, V. Specchia, Catal. Today 119 (2007) 228–232.
[17] N. Sahli, C. Petit, A.C. Roger, A. Kiennemann, S. Libs, M.M. Bettahar, Catal. Today 113 (2006) 187–193.
[18] M.D. Shibanova, A.V. Golub'ev, Y.V. Maksimov, I.P. Suzdalev, V.N. Korchak, Kinet. Catal. 42 (2001) 112–116.
[19] I. Spassova, D. Mehandjiev, React. Kinet. Catal. Lett. 69 (2000) 231–237.
[20] Y. Tanaka, T. Utaka, R. Kikuchi, T. Takeguchi, K. Sasaki, K. Eguchi, J. Catal. 215 (2003) 271–278.
[21] P. Thormahlen, E. Fridell, N. Cruise, M. Skoglundh, A. Palmqvist, Appl. Catal. B: Environ. 31 (2001) 1–12.
[22] J.H. Tong, L.L. Bo, Z. Li, Z.Q. Lei, C.G. Xia, J. Mol. Catal. A-Chem. 307 (2009) 58–63.
[23] A. Urda, A. Herraiz, A. Redey, I.C. Marcu, Catal. Commun. 10 (2009) 1651–1655.
[24] T. Valdes-Solis, G. Marban, A.B. Fuertes, Catal. Today 116 (2006) 354–360.
[25] L. Yan, T. Ren, X.L. Wang, Q. Gao, D. Ji, J.S. Suo, Catal. Commun. 4 (2003) 505–509.
[26] M.H. Zahir, S. Katayama, M. Awano, Mater. Chem. Phys. 86 (2004) 99–104.
[27] R. Strobel, S.E. Pratsinis, J. Mater. Chem. 17 (2007) 4743–4756.
[28] C.R. Bickmore, K.F. Waldner, D.R. Treadwell, R.M. Laine, J. Am. Ceram. Soc. 79 (1996) 1419–1423.
[29] J.A. Azurdia, J. Marchal, P. Shea, H.P. Sun, X.Q. Pan, R.M. Laine, Chem. Mater. 18 (2006) 731–739.
[30] J.R. Jensen, T. Johannessen, S. Wedel, H. Livbjerg, J. Nanopart. Res. 2 (2000) 363–373.
[31] N. van Vegten, M. Maciejewski, F. Krumeich, A. Baiker, Appl. Catal. B: Environ. 93 (2009) 38–49.
[32] W.R. Moser, K.E. Connolly, Chem. Eng. J. 64 (1996) 239–246.
[33] H.M.J. Kusar, A.G. Ersson, S.G. Jaras, Appl. Catal. B: Environ. 45 (2003) 1–11.
[34] T.V. Choudhary, S. Banerjee, V.R. Choudhary, Appl. Catal. A: Gen. 234 (2002) 1–23.
[35] S. Arnone, G. Bagnasco, G. Busca, L. Lisi, G. Russo, M. Turco, Stud. Surf. Sci. Catal., Elsevier, 1998, pp. 65–70.
[36] J. Cheng, J.J. Yu, X.P. Wang, L.D. Li, J.J. Li, Z.P. Hao, Energy Fuels 22 (2008) 2131–2137.
[37] D. Fino, S. Solaro, N. Russo, G. Saracco, V. Specchia, Top. Catal. 42–43 (2007) 449–454.
[38] P.E. Marti, M. Maciejewski, A. Baiker, Appl. Catal. B: Environ. 4 (1994) 225–235.
[39] N. van Vegten, D. Ferri, M. Maciejewski, F. Krumeich, A. Baiker, J. Catal. 249 (2007) 269–277.
[40] R. Strobel, S.E. Pratsinis, A. Baiker, J. Mater. Chem. 15 (2005) 605–610.
[41] S. Roy, N. van Vegten, A. Baiker, J. Catal. 271 (2010) 125–131.
[42] L. Madler, W.J. Stark, S.E. Pratsinis, J. Mater. Res. 17 (2002) 1356–1362.
[43] NIST X-ray Photoelectron Spectroscopy Database, Version 3.5 (National Institute of Standards and Technology, Gaithersburg, 2003), http://srdata.nist.gov/xps/.
[44] D. Briggs, M.P. Seah (Eds.), Practical Surface Analysis by Auger and X-ray Photoelectron Spectroscopy, John Wiley & Sons, New York, 1983.
[45] M.J. Iqbal, S. Farooq, Mater. Sci. Eng. B-Solid State Mater. Adv. Technol. 136 (2007) 140–147.

[46] R.D. Shannon, C.T. Prewitt, Acta Crystallogr. Sect. B 25 (1969) 925.
[47] M. Zawadzki, W. Staszak, F.E. Lopez-Suarez, M.J. Illan-Gomez, A. Bueno-Lopez, Appl. Catal. A: Gen. 371 (2009) 92–98.
[48] Y.H. Xu, H. Zhang, X. Duan, Y.P. Ding, Mater. Chem. Phys. 114 (2009) 795–801.
[49] W. Zhang, H.L. Tay, S.S. Lim, Y.S. Wang, Z.Y. Zhong, R. Xu, Appl. Catal. B: Environ. 95 (2010) 93–99.
[50] D.E. Haycock, C.J. Nicholls, D.S. Urch, M.J. Webber, G. Wiech, J. Chem. Soc. - Dalton Trans. (1978) 1785–1790.
[51] V. Dicastro, G. Polzonetti, J. Electron Spectrosc. Relat. Phenom. 48 (1989) 117–123.
[52] M. Oku, K. Hirokawa, S. Ikeda, J. Electron Spectrosc. Relat. Phenom. 7 (1975) 465–473.
[53] Y. Umezawa, C.N. Reilley, Anal. Chem. 50 (1978) 1290–1295.
[54] E.R. Stobbe, B.A. de Boer, J.W. Geus, Catal. Today 47 (1999) 161–167.
[55] W.K. Jozwiak, E. Kaczmarek, T.P. Maniecki, W. Ignaczak, W. Maniukiewicz, Appl. Catal. A: Gen. 326 (2007) 17–27.
[56] G. Jacobs, T.K. Das, Y.Q. Zhang, J.L. Li, G. Racoillet, B.H. Davis, Appl. Catal. A: Gen. 233 (2002) 263–281.
[57] F. Kapteijn, A.D. Vanlangeveld, J.A. Moulijn, A. Andreini, M.A. Vuurman, A.M. Turek, J.M. Jehng, I.E. Wachs, J. Catal. 150 (1994) 94–104.
[58] H.Y. Wang, E. Ruckenstein, Appl. Catal. A: Gen. 209 (2001) 207–215.